LANGMUIR

pubs.acs.org/Langmuir Article

Poloxamer 407 and DMPC Form Large Lipid Nanodiscs: Structural Characterization Using Small-Angle X-ray Scattering

Masakazu Fukuda,* Yuichi Takasaki, Mizuho Ichihara, Toru Takarada, Keisuke Ikeda, Minoru Nakano, and Masafumi Tanaka*

Cite This: *Langmuir* 2025, 41, 17902−17913

Read Online

ACCESS | Metrics & More | Article Recommendations | Supporting Information

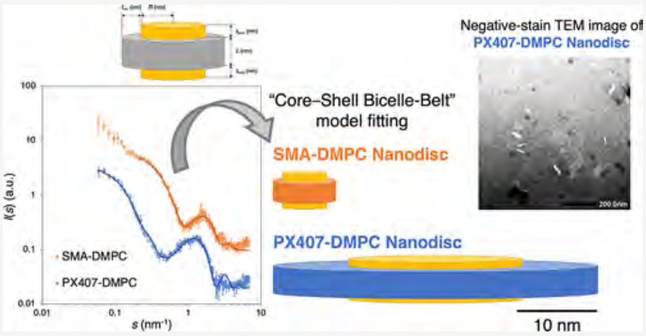

ABSTRACT: Lipid nanodiscs (LNDs) provide versatile platforms for membrane protein research and function as innovative drug delivery systems. This study presents the structural characterization of LNDs composed of poloxamer 407 (PX407) and 1,2-dimyristoyl-*sn*-glycero-3-phosphocholine (DMPC) using small-angle X-ray scattering (SAXS) analysis, further supported by turbidity assessment and transmission electron microscopy observation. Among the evaluated poloxamers, PX407, which contains the highest proportion of hydrophobic poly(propylene oxide) segment, exhibited superior DMPC solubilization capability. SAXS analysis, employing the core−shell bicelle-belt model, indicated that PX407-DMPC mixtures formed discoidal nanostructures. These structures preserved membrane thickness comparable to conventional phospholipid bilayers while achieving core diameters of 17−30 nm—over three times larger than those of styrene-maleic acid−based LNDs under similar conditions. The dimensions were systematically regulated by salt concentration and polymer-to-lipid ratio, with greater stability observed at higher polymer content (PX407: DMPC = 2:1 mass ratio) and elevated salt concentrations (≥300 mM NaCl). Although these LNDs appeared to be unstable above the DMPC gel-to-liquid crystalline phase transition temperature (∼24 °C), their larger size and temperature-responsive properties suggest potential applications in membrane protein research requiring extensive lipid platforms and in systems benefiting from temperature-dependent behavior.

■ INTRODUCTION

Lipid nanodiscs (LNDs) are self-assembled nanostructures composed of a phospholipid (PL) bilayer stabilized by amphiphilic scaffolding molecules. These nanoscale systems have garnered increasing attention for serving as platforms for membrane protein structural and functional studies, and acting as innovative drug delivery vehicles.[1−3] In membrane protein research, LNDs provide a native-like lipid environment that preserves protein structure and function. From a drug delivery perspective, their well-defined size and discoidal morphology enhance tissue penetration and cellular uptake while minimizing rapid renal clearance.

The development of LND technology originated from studies on high-density lipoproteins (HDLs), naturally occurring discoidal particles responsible for lipid transport in blood circulation.[4−9] Membrane scaffold proteins (MSPs) were created as engineered variants of apolipoprotein A-I, a key component of HDL.[10,11] MSP-based LNDs have advanced membrane protein structural biology, facilitating studies of various membrane proteins, including G protein-coupled receptors and ion channels.[12−15] However, MSP-based and extended MSP-based LNDs encountered limitations: constraints on incorporating large membrane proteins due to size limits up to approximately 17 nm,[16,17] detergent requirements during reconstitution that could compromise protein stability, and high production costs. To address these challenges, styrene-maleic acid (SMA) was introduced as an alternative scaffold, offering direct extraction of membrane proteins from lipid bilayers without detergents.[18−20] SMA is a copolymer composed of styrene and maleic acid units, where styrene provides hydrophobicity, and maleic acid contributes hydrophilicity to the polymer chain (Figure 1a). Subsequently, second-generation synthetic polymers offering unique advantages were developed.[21−23] Strategies to overcome size limitations were also reported.[24−26]

As drug delivery vehicles, LNDs possess distinct advantages due to their HDL-inspired design, exhibiting excellent biocompatibility and stability in blood circulation. Their nanoscale dimensions are suitable for efficient tissue

Received: April 3, 2025
Revised: May 31, 2025
Accepted: June 26, 2025
Published: July 4, 2025

https://doi.org/10.1021/acs.langmuir.5c01675

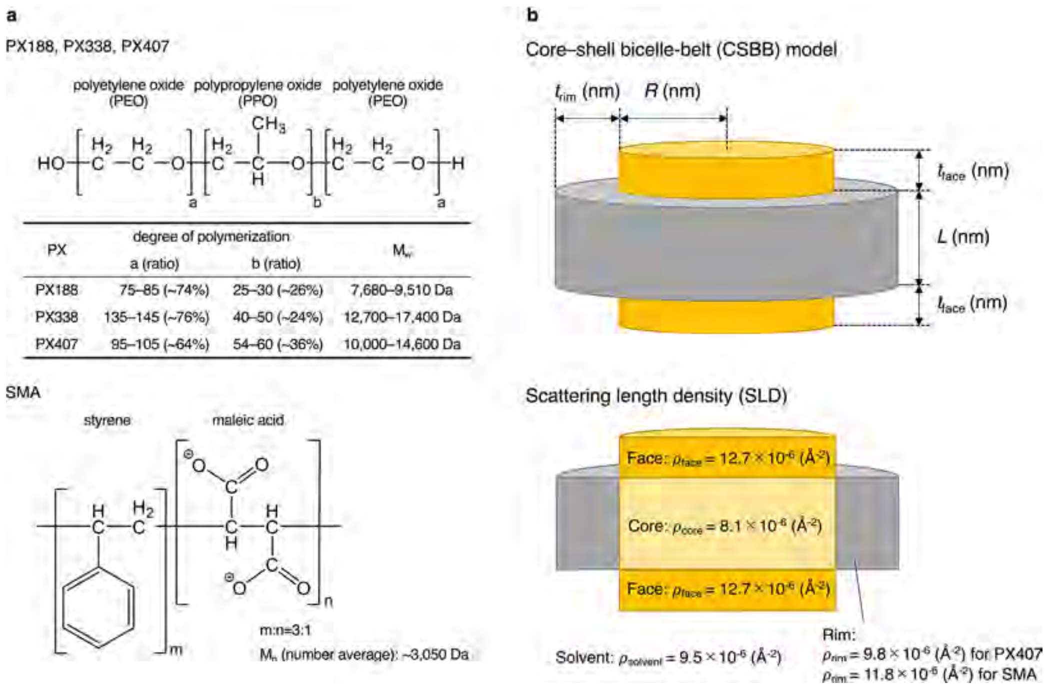

PX	degree of polymerization a (ratio)	 b (ratio)	M_w
PX188	75–85 (~74%)	25–30 (~26%)	7,680–9,510 Da
PX338	135–145 (~76%)	40–50 (~24%)	12,700–17,400 Da
PX407	95–105 (~64%)	54–60 (~36%)	10,000–14,600 Da

Figure 1. Structural formulas of the amphiphilic polymers used in this study and the core–shell bicelle-belt (CSBB) model employed for SAXS data analysis. (a) Structural formulas of poloxamer triblock copolymers (PX188, PX338, and PX407), comprising hydrophilic poly(ethylene oxide) (PEO) and hydrophobic poly(propylene oxide) (PPO) blocks, are shown along with their degrees of polymerization and molecular weights. The structure of the styrene-maleic acid (SMA) copolymer consisting of styrene (m) and maleic acid (n) units in a 3:1 molar ratio and its number-average molecular weight are also presented. (b) A schematic representation of the CSBB model illustrates key dimensional parameters (R, t_{rim}, t_{face}, and L) and the scattering length density (SLD) values for various components. The core region (light yellow), face regions (yellow), and rim region (gray) are characterized by distinct SLD values, with the rim exhibiting polymer-specific SLD values for PX407 and SMA.

penetration and cellular uptake while remaining large enough to avoid rapid renal clearance.[27,28] Additionally, their discoidal morphology enhances cellular interactions compared to spherical particles, promoting efficient cellular internalization.[29,30] LNDs exhibited versatility in carrying various payloads, including hydrophobic small-molecule drugs,[31−34] nucleic acid therapeutics,[35−37] and imaging probes.[38−41] However, translation to clinical applications faces key challenges. First, scaffold molecules must meet stringent safety standards for pharmaceutical applications, creating a demand for biocompatible synthetic polymers with established safety profiles. Second, conventional LNDs exhibit limited drug-loading capacity due to their relatively small size, highlighting the need for size optimization strategies.

Among the amphiphilic polymers used as pharmaceutical excipients are poloxamers (PXs), characterized by their triblock copolymer structure, consisting of a hydrophobic poly(propylene oxide) (PPO) block in the center and hydrophilic poly(ethylene oxide) (PEO) blocks at both ends (Figure 1a). The relative proportions of PEO and PPO blocks critically determine their physicochemical properties. Wu et al. (2009) demonstrated that these amphiphilic polymers could transform PL liposomes into bilayer discs with diameters of approximately 30−100 nm, as observed using cryo-transmission electron microscopy. Specifically, Poloxamer 338 (PX338) formed LNDs below the gel-to-liquid crystalline phase transition temperature (T_m). Wu et al. proposed a mechanism wherein PX338 molecules, separated from gel-phase lipid domains, accumulate at domain boundaries, resulting in the disruption of PL vesicle structures and the formation of discoidal structures.[42,43] Despite observing temperature-dependent transformations, fundamental questions remain about the precise molecular mechanisms governing PX-based LND formation and stability, including the roles of polymer-to-lipid ratios, salt concentrations, and molecular interactions at the disc edges. Furthermore, the comprehensive structural characteristics of these nanosized discs remain insufficiently characterized.

In this study, we characterized the structural features of PX-stabilized LNDs, focusing on Poloxamer 407 (PX407), which possesses unique amphiphilic properties with a high proportion of hydrophobic segment. Through small-angle X-ray scattering (SAXS) analysis combined with turbidity assessment and transmission electron microscopy (TEM) observation, we investigated how parameters such as temperature, salt concentration, and polymer-to-lipid ratio affected the formation and properties of these LNDs. Our findings provided detailed structural information on PX407-stabilized LNDs and their thermal stability and size control, thereby enhancing the understanding of their potential applications in membrane protein research and drug delivery systems.

■ MATERIALS AND METHODS

Materials. 1,2-Dimyristoyl-*sn*-glycero-3-phosphocholine (DMPC) was purchased from NOF Corporation (Tokyo, Japan), and 1-palmitoyl-2-oleoyl-*sn*-glycero-3-phosphocholine (POPC) was obtained from Avanti Polar Lipids (Alabaster, AL, USA). Poloxamer 188 (PX188), Poloxamer 338 (PX338), and Poloxamer 407 (PX407) were generously provided by BASF (Ludwigshafen, Germany). SMA Copolymer 3:1, prehydrolyzed (Lipodisq) was purchased from Sigma-Aldrich (St. Louis, MO, USA). The SMA used in this study is a hydrolyzed copolymer consisting of styrene and maleic acid units in a 3:1 molar ratio. The structural formulas and molecular weights of

PX188, PX338, PX407, and SMA are shown in Figure 1a. All other chemicals were purchased from FUJIFILM Wako Pure Chemical Corporation (Osaka, Japan).

Sample Preparation. DMPC and POPC were dissolved in chloroform at concentrations of 10.9 and 19.8 mg/mL, respectively. The PL concentrations were determined through phosphorus quantification using the Bartlett method.[44]

To prepare PX–PL mixtures, 4 mg of DMPC or POPC was placed in a round-bottom flask. The chloroform was removed using a rotary evaporator and followed by overnight vacuum drying to ensure complete solvent removal. The resulting lipid film was hydrated by vortexing with 500 μL of PX solutions (8 mg/mL PX188, 8 mg/mL PX338, or 4, 8, or 16 mg/mL PX407 in 10 mM sodium phosphate, 150, 300, or 600 mM NaCl, 0.1 mg/mL NaN_3, pH 7.4) at room temperature (nominally 23 °C). The concentrations of DMPC and POPC were determined using a PL quantification kit (LabAssay Phospholipid, FUJIFILM Wako Pure Chemical Corporation) and were confirmed to be between 7.4 and 9.6 mg/mL. The samples were stored at 4 °C.

To prepare the SMA-DMPC mixture, a dried DMPC film (4 mg) was hydrated by vortexing with 500 μL of buffer (10 mM sodium phosphate, 300 mM NaCl, 0.1 mg/mL NaN_3, pH 7.4). The resulting suspension was extruded 31 times through a polycarbonate membrane with a 100 nm pore size to form predominantly unilamellar vesicles approximately 100 nm in diameter, although some multilamellar structures may remain due to the absence of freeze–thaw cycles.[45,46] A solution of SMA (14.6 mg/mL) was prepared in the same buffer. The SMA solution was then mixed with the liposome suspension at room temperature (nominally 23 °C) to achieve final concentrations of 7.3 and 3.65 mg/mL for SMA and DMPC, respectively. After incubation at room temperature for over 1 h, the sample was subjected to SAXS measurements.

Dynamic Light Scattering (DLS). DLS measurements were conducted using an in situ, contactless DLS analyzer (Vasco Kin, Cordouan Technologies, Pessac, France) at room temperature (nominally 23 °C). The hydrodynamic diameters of the samples were measured directly in storage tubes. The scattered light was detected at an angle of 170° (backscattering mode). The resulting autocorrelation functions were analyzed using the cumulant method, assuming a refractive index of 1.33 (for water) for the solvent, to determine the number-weighted mean particle diameter.

Small-Angle X-ray Scattering (SAXS). SAXS experiments were conducted using a SAXSpace system (Anton Paar, Graz, Austria) with line-collimated Cu Kα radiation ($\lambda = 0.1542$ nm). The samples were loaded into 1 mm quartz capillary cells and thermostated at 5, 10, 20, 30, or 40 °C using a Peltier-controlled sample holder (TCStage 150, Anton Paar). One-dimensional scattering intensities [$I(s)$] were recorded using a 1D-diode array detector (Mythen 1K, Dectris, Baden-Dättwil, Switzerland) positioned at a sample–detector distance of 317.1 mm. A momentum transfer range of $0.05 < s < 7.55\ \mathrm{nm}^{-1}$ (where $s = 4\pi\sin\theta/\lambda$, 2θ is the scattering angle) was covered. For all experiments, the attenuated primary beam at $s = 0$ was monitored using a semitransparent beam stop. SAXS patterns were calibrated for transmission by normalizing the zero-s primary intensity to unity. Data from three consecutive 10 min frames were averaged for each sample and buffer. Background subtraction (including contribution from the capillary and corresponding buffer) and collimation correction (desmearing) were performed using SAXSanalysis software (Anton Paar).

Assuming no interaction between particles in the system [i.e., the structure factor $S(s) = 1$], the $I(s)$ is given by Fourier transformation of the pair-distance distribution function of the particle, $p(r)$, as

$$I(s) = 4\pi \int_0^{\infty} p(r)\frac{\sin(sr)}{sr}dr \tag{1}$$

where r is the distance between two scattering centers selected within the particle. The indirect Fourier transformation (IFT) technique was used to calculate $p(r)$ and determine the maximum dimension [$D_{\max}$ (nm)] of the particles.[47,48] The analysis was performed using the PCG GIFT software (version 4.0, University of Graz). Additionally, the radius of gyration [R_g (nm)] was obtained from $p(r)$ using the following equation:[49]

$$R_g = \sqrt{\frac{\int_0^{D_{\max}} p(r)r^2dr}{2\int_0^{D_{\max}} p(r)dr}} \tag{2}$$

Assuming a flat structure with constant thickness and an extension much greater than the thickness, $I(s)$ can be expressed as[49]

$$I(s) = \frac{2\pi A}{s^2}I_t(s) \tag{3}$$

where, A is the area of the lamellar particles and $I_t(s)$ is the thickness contribution. $I_t(s)$ is related to the thickness pair-distance distribution function [$p_t(r)$] by

$$I_t(s) = 2\int_0^{\infty} p_t(r)\cos(sr)dr \tag{4}$$

The thickness of the lamellar particle [T (nm)] and the thickness pair-distance distribution function $p_t(r)$ were determined using the IFT method for flat structures,[47,48] implemented in the PCG GIFT software (version 4.0, University of Graz).

The hypothesis that the PX407-DMPC system exhibits a discoidal structure was tested by evaluating whether the theoretically calculated radius of gyration [R_g^{disc} (nm)], assuming a homogeneous discoidal structure, matches the experimentally obtained R_g from standard IFT analysis. The R_g^{disc} was estimated using the $D_{\max}$ (nm) and T (nm) parameters obtained from standard IFT analysis and IFT analysis assuming flat structures, respectively, with the following equation:[49]

$$R_g^{\mathrm{disc}} = \sqrt{\frac{D^2}{8} + \frac{T^2}{12}} \tag{5}$$

where, D is the diameter of the discoidal particles, which can be calculated as $D = \sqrt{D_{\max}^2 - T^2}$.

The SAXS data were analyzed by fitting them to the core–shell bicelle-belt (CSBB) model, as illustrated in Figure 1b, using the SasView software (version 5.0.6, www.sasview.org).[50,51] In the CSBB model, the scattering intensity $I(s)$ is expressed using the corresponding form factor $F_{\mathrm{CSBB}}(s, \alpha)$ as follows:[52]

$$I(s) = \frac{\mathrm{scale}}{V_t}\int F_{\mathrm{CSBB}}(s, \alpha)^2\sin(\alpha)d\alpha + \mathrm{background} \tag{6}$$

where α represents the angle between the scattering vector s and the cylinder axis of the particle, and V_t denotes the total volume of the particle. The form factor $F(s, \alpha)$ is given by[52]

$$\begin{aligned} F_{\mathrm{CSBB}}(s, \alpha) = \{&(\rho_{\mathrm{core}} - \rho_{\mathrm{rim}} - \rho_{\mathrm{face}} + \rho_{\mathrm{solvent}}) \\ &V_c\frac{2J_1(sR\sin\alpha)}{sR\sin\alpha}\frac{\sin[s(L/2)\cos\alpha]}{s(L/2)\cos\alpha} + (\rho_{\mathrm{face}} - \rho_{\mathrm{solvent}}) \\ &V_{c+f}\frac{2J_1(sR\sin\alpha)}{sR\sin\alpha}\frac{\sin[s(L/2 + t_{\mathrm{face}})\cos\alpha]}{s(L/2 + t_{\mathrm{face}})\cos\alpha} \\ &+ (\rho_{\mathrm{rim}} - \rho_{\mathrm{solvent}})V_{c+r}\frac{2J_1[s(R + t_{\mathrm{rim}})\sin\alpha]}{s(R + t_{\mathrm{rim}})\sin\alpha} \\ &\frac{\sin[s(L/2)\cos\alpha]}{s(L/2)\cos\alpha}\} \end{aligned} \tag{7}$$

where ρ_{core}, ρ_{face}, ρ_{rim}, and ρ_{solvent} represent the scattering length densities (SLDs) of the hydrophobic core, hydrophilic face, rim, and solvent, respectively. The structural parameters R, L, t_{face}, and t_{rim} denote the radius of the core, the thickness of core, the thickness of the face, and the thickness of the rim, respectively. V_c, V_{c+f}, V_{c+r}, and V_t represent the volume of the core, the combined volume of the core and face, the combined volume of the core and rim, and the total particle volume, respectively. J_1 is the first-order Bessel function of the first kind. The SLD values for the core [$\rho_{\mathrm{core}} = 8.1 \times 10^{-6}$ (Å^{-2})] and face [ρ_{face} = 12.7 × 10^{-6} (Å^{-2})] were adopted from literature values corresponding to the acyl chain region and polar headgroup of DMPC bilayers.[53] The rim SLD values [ρ_{rim} = 9.8 × 10^{-6} (Å^{-2}) for PX407 and 11.8 × 10^{-6} (Å^{-2}) for SMA] were calculated based on the molecular weights [12,151 Da for PX407 (corresponding to a = 101, b = 56) and 3,050 Da for SMA] and densities (1.06 g/cm^3 for PX407 and 1.298 g/cm^3 for SMA) of the respective polymers. These molecular weights and densities were obtained from their technical/product information sheets. The solvent SLD [$\rho_{solvent}$ = 9.5 × 10^{-6} (Å^{-2})] was calculated based on the solvent composition. These values are summarized in Figure 1b. To improve the fitting results, the polydispersity of R was considered in the fitting procedure among the four structural parameters R, L, t_{face}, and t_{rim}.

Transmission Electron Microscopy (TEM). PX407-DMPC samples were diluted 5-fold with the corresponding buffer solution. A heat block set at 23 °C was covered with Parafilm, and 20 μL droplets of sample solution and staining solution (4-fold diluted EM stainer, Nisshin EM, Tokyo, Japan) were placed separately on the surface. A carbon film-supported Cu grid (Filgen, Nagoya, Japan) was placed on the sample solution droplet and left for 2 min. Excess sample solution was removed from the grid using filter paper, after which the grid was negatively stained with the staining solution for 30 s. Excess staining solution was removed using filter paper, and the grid was air-dried. TEM images were obtained using a JEM-1400TC transmission electron microscope (JEOL, Tokyo, Japan) operating at an acceleration voltage of 80 kV.

RESULTS AND DISCUSSION

Turbidity Assessment of Poloxamer-Phospholipid Systems. The visual appearance of the PX–PL mixtures provided initial insights into their assembly behavior. Photographs were taken shortly after the samples equilibrated to room temperature (nominally 23 °C) from storage at 4 °C (Figure 2a–d). Comparison of different PXs at a fixed PX:DMPC mass ratio of 1:1 in 300 mM NaCl revealed a distinct turbidity trend: PX188 > PX338 > PX407, with PX407-containing samples exhibiting notable transparency (Figure 2a). This observation aligns with the molecular structure of PX407, which contains the highest proportion of the hydrophobic PPO segment among the tested PXs, resulting in superior solubilization capability. Notably, despite similar PPO content, PX338 exhibited superior solubilization compared to PX188, likely due to its higher molecular weight and, consequently, a greater number of PO units. These findings highlight how variations in PPO content and molecular weight among different PXs significantly influence their PL solubilization capacity.

Given its superior solubilization properties, PX407 was selected for a systematic investigation of parameters affecting PL solubilization, including salt concentration, temperature, the PX407-to-PL mass ratio, and PL species. At a fixed PX407:DMPC mass ratio of 1:1, increasing NaCl concentration from 150 to 300 or 600 mM resulted in transparent solutions, while slight turbidity was observed at 150 mM (Figure 2b). Varying the PX407: DMPC mass ratio (0.5:1, 1:1, and 2:1) in 300 mM NaCl yielded transparent solutions at ratios ≥ 1:1, with slight turbidity at 0.5:1 (Figure 2c). Substituting DMPC with POPC at PX407:PL = 1:1 in 300 mM NaCl led to pronounced turbidity (Figure 2d). Collectively, these observations indicate optimal DMPC solubilization at salt concentrations ≥ 300 mM and PX407: DMPC mass ratios ≥ 1:1, while substitution with POPC substantially impedes solubilization. These findings are explained by the strengthening of hydrophobic interactions at higher salt concentrations and the greater hydrophobicity of POPC compared to DMPC due to its longer acyl chains.

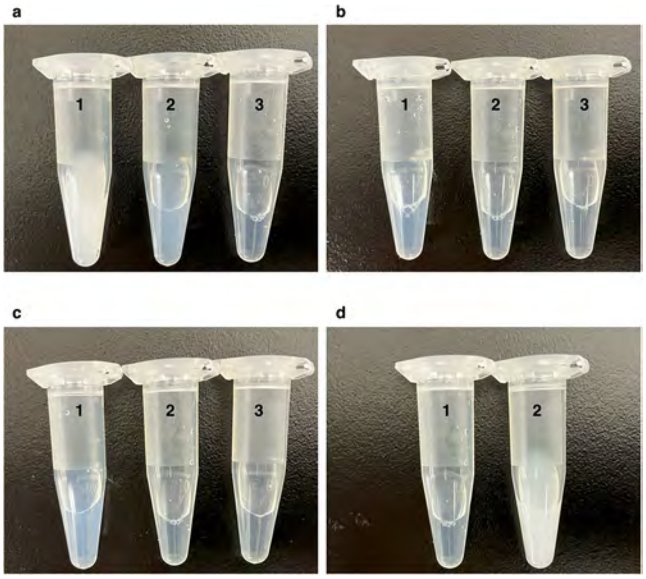

Figure 2. Effects of various parameters on the solution characteristics of poloxamer-phosphatidylcholine mixtures. (a) Effect of poloxamer type [(1) PX188, (2) PX338, and (3) PX407] on DMPC solubilization at a 1:1 mass ratio in 300 mM NaCl. (b) Effect of NaCl concentration [(1) 150 mM, (2) 300 mM, and (3) 600 mM] on PX407-DMPC solubilization at a 1:1 mass ratio. (c) Effect of mass ratio [(1) 0.5:1, (2) 1:1, and (3) 2:1] on PX407-DMPC solubilization in 300 mM NaCl. (d) Effect of phosphatidylcholine type [(1) DMPC and (2) POPC] on PX407-mediated solubilization at a 1:1 mass ratio in 300 mM NaCl. The concentrations of PL were between 7.4 and 9.6 mg/mL.

To quantitatively corroborate these visual observations, the hydrodynamic sizes and size distributions of the assemblies were measured using DLS (Table 1). The DLS results strongly correlated with the visual assessments: samples exhibiting pronounced turbidity had large mean diameters (398–2629 nm), those with slight turbidity had intermediate sizes (43–60 nm), and transparent samples had the smallest dimensions (23–33 nm). The particle size number distributions for each sample are shown in Figure S1, while autocorrelation functions and cumulant fitting results are presented in Figure S2. The corresponding PDI values are listed in Table 1. At 300 mM NaCl and a mass ratio of PX:DMPC = 1:1, PX407 exhibited a relatively narrow size distribution (PDI = 0.30), while PX188 and PX338 showed low PDI values (0.07 and 0.03, respectively) despite differences in visual turbidity. At a mass ratio of PX407:DMPC = 1:1, when the NaCl concentration was varied from 150 to 600 mM, PDI values ranged from 0.23 to 0.30, indicating acceptable size distribution control. When the mass ratio of PX407 and DMPC (0.5:1, 1:1, 2:1) was varied in 300 mM NaCl, the 2:1 ratio showed the narrowest distribution (PDI = 0.20). At 300 mM NaCl and PX407:PL = 1:1, POPC (PDI = 0.32) exhibited higher polydispersity than DMPC (PDI = 0.30).

SAXS Analysis of PX407/SMA-DMPC Systems: Standard IFT Approach. To elucidate the structure of particles formed by PX407-DMPC mixing, SAXS measurements were performed under various conditions, examining the effects of salt concentration, the PX407-to-DMPC mass ratio, and temperature. Three SAXS measurements, each lasting 10 min, were performed for each sample. No clear time-dependent changes in the SAXS profiles were observed during

Table 1. Mean Diameters (nm) and PDI Obtained from DLS Measurements

					DLS data	
polymer	lipid	NaCl conc. (mM)	mass ratio (polymer: lipid)	temperature (°C)	mean diameter (nm)[b]	PDI
PX188	DMPC	300	1:1	R.T.[a]	2629	0.07
PX338	DMPC	300	1:1	R.T.[a]	398	0.03
PX407	DMPC	300	1:1	R.T.[a]	30	0.30
PX407	DMPC	150	1:1	R.T.[a]	43	0.23
PX407	DMPC	300	1:1	R.T.[a]	30	0.30
PX407	DMPC	600	1:1	R.T.[a]	23	0.24
PX407	DMPC	300	1:0.5	R.T.[a]	60	0.27
PX407	DMPC	300	1:1	R.T.[a]	30	0.30
PX407	DMPC	300	2:1	R.T.[a]	33	0.20
PX407	DMPC	300	1:1	R.T.[a]	30	0.30
PX407	POPC	300	1:1	R.T.[a]	575	0.32

[a] Nominally 23 °C. [b] Obtained from the particle number distribution calculated using cumulant analysis.

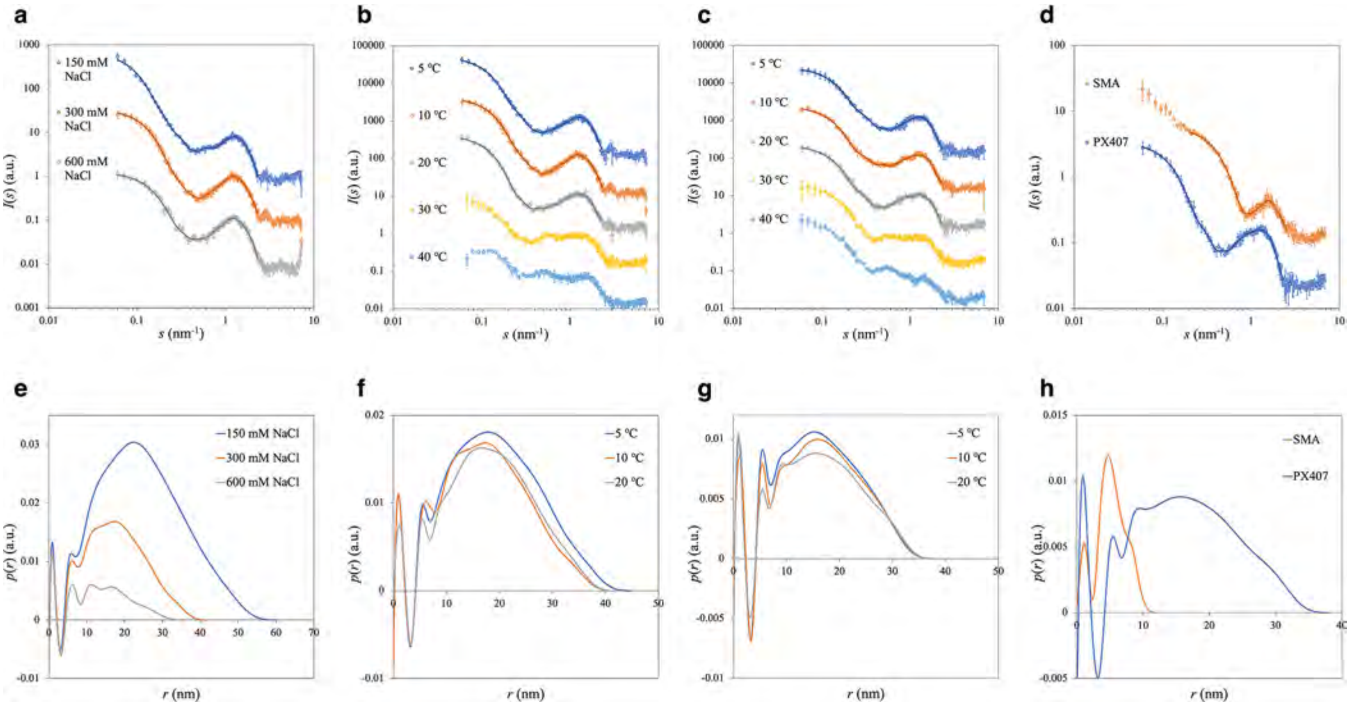

Figure 3. SAXS profiles and pair-distance distribution functions $p(r)$ of PX407-DMPC and SMA-DMPC systems under various conditions. (a–d) SAXS profiles (dots) with the theoretical scattering curves (solid lines) obtained from standard IFT analysis, and (e–h) corresponding $p(r)$ functions. SAXS profiles are presented as mean ± standard deviation ($n = 3$). (a,e) Effect of NaCl concentration (150, 300, and 600 mM) on PX407-DMPC (1:1 mass ratio) systems at 10 °C. (b,f) Effect of temperature (5–40 °C) on PX407-DMPC systems (PX407: DMPC = 1:1 mass ratio) in 300 mM NaCl. (c,g) Effect of temperature (5–40 °C) on PX407-DMPC systems (PX407: DMPC = 2:1 mass ratio) in 300 mM NaCl. (d,h) Effect of amphiphilic polymer type (SMA and PX407) on polymer-DMPC systems (polymer: DMPC = 2:1 mass ratio) in 300 mM NaCl at 20 °C. The concentrations of DMPC were 7.4–9.6 mg/mL for PX407-DMPC systems and 3.65 mg/mL for SMA-DMPC system.

these three measurements, suggesting that the samples remained stable for at least 30 min at each temperature. Additionally, samples containing SMA instead of PX407 were analyzed for comparison. The SMA-DMPC mixtures have been extensively studied, and it is well established that SMA solubilizes DMPC liposomes at T_m of DMPC (approximately 24 °C), forming LNDs with a diameter of 8–10 nm.[54] Figure 3a–d present the scattering curves along with the theoretical curves obtained from standard IFT analysis, while Figure 3e–h show the corresponding pair-distance distribution functions, $p(r)$. All SAXS patterns of the PX407-DMPC systems are similar to those of SMA-DMPC system, suggesting that the PX407-DMPC systems also consist of LNDs. The $p(r)$ functions obtained from the standard IFT analysis show oscillatory patterns in the low-r region, reflecting the characteristic distances between areas with positive and negative SLD within the membrane.

The effect of salt concentration was first examined at 10 °C with a PX407: DMPC mass ratio of 1:1 (Figure 3a,e). The scattering intensity in the low-s region ($s < 0.3$ nm^{-1}) varied notably with salt concentration. The radius of gyration, R_g, decreased from 19 to 14 to 12 nm as NaCl concentration increased from 150 to 300 to 600 mM, with corresponding D_{max} values of 60, 42, and 34 nm, respectively (Table 2). Although R_g is typically determined through Guinier analysis, in this study we calculated R_g from $p(r)$ to mitigate potential influences on scattering intensity in the low-s region caused by remaining DMPC vesicles.[55]

Table 2. R_g (nm), $D_{\max}$ (nm), Thickness [T (nm)], and R_g^{disc} (nm) Obtained from SAXS Measurements

					SAXS data			
					IFT (standard)		IFT (flat structure)	discoidal structure[a]
polymer	lipid	NaCl conc. (mM)	mass ratio (polymer: lipid)	temperature (°C)	R_g (nm)[b]	$D_{\max}$ (nm)[c]	thickness (T) (nm)[d]	R_g^{disc} (nm)[e]
PX407	DMPC	150	1:1	10	19	60	5.5	21
PX407	DMPC	300	1:1	10	14	42	5.5	15
PX407	DMPC	600	1:1	10	12	34	5.5	12
PX407	DMPC	300	1:1	5	15	45	5.5	16
PX407	DMPC	300	1:1	10	14	42	5.5	15
PX407	DMPC	300	1:1	20	14	42	5.5	15
PX407	DMPC	300	1:1	30	N.A.	N.A.	N.A.	N.A.
PX407	DMPC	300	1:1	40	N.A.	N.A.	N.A.	N.A.
PX407	DMPC	300	2:1	5	13	38	5.5	13
PX407	DMPC	300	2:1	10	13	38	5.5	13
PX407	DMPC	300	2:1	20	13	38	5.5	13
PX407	DMPC	300	2:1	30	N.A.	N.A.	N.A.	N.A.
PX407	DMPC	300	2:1	40	N.A.	N.A.	N.A.	N.A.
SMA	DMPC	300	2:1	20	4	12	5.0	4
PX407	DMPC	300	2:1	20	13	38	5.5	13

[a] The homogeneous discoidal structure with diameter D (nm) and thickness T (nm) was assumed, where D was determined from $D = \sqrt{D_{\max}{}^2 - T^2}$. [b] Calculated using eq 2. [c] Determined using standard IFT method. [d] Determined using IFT method for flat structures. [e] Calculated using eq 5.

The temperature dependence was investigated at both 1:1 and 2:1 PX407: DMPC mass ratios in 300 mM NaCl (Figure 3b,c,f,g). At the 1:1 ratio, the particle structure showed slight variations between 5 and 20 °C, with R_g values ranging from 14 to 15 nm and $D_{\max}$ values from 42 to 45 nm (Table 2). In contrast, at the 2:1 ratio, the structural parameters remained consistent (R_g = 13 nm and $D_{\max}$ = 38 nm) throughout this temperature range (Table 2), suggesting enhanced particle stability at higher PX407 content. However, at temperatures above 20 °C, significant structural changes occurred in both systems, preventing meaningful determination of these parameters. This destabilization above 20 °C was likely attributed to the gel-to-liquid crystalline phase transition of DMPC, which occurs at approximately 24 °C.[42] Visual observation also revealed sample turbidity when the temperature was raised to 30 °C (data not shown).

Comparison of the PX407- and SMA-based systems at 20 °C (Figure 3d,h) revealed distinct structural differences. The characteristic peak attributed to the PL bilayer structure appeared at $s \approx 1.6$ nm^{-1} for the SMA system, while it appeared at $s \approx 1.2$ nm^{-1} for the PX407 system. This suggests that the PX407 system possesses a thicker membrane structure than the SMA system. Bjørnestad et al. reported SAXS profiles of SMA-DMPC LNDs and DMPC liposomes at 18 °C,[56] and the peak positions observed in our SMA and PX407 systems closely matched those reported for SMA-DMPC LNDs and DMPC liposomes, respectively. This supports the conclusion that the PX407 system maintains a membrane thickness more similar to that of conventional lipid bilayers compared to the SMA system.

The SMA-DMPC system formed smaller particles, with R_g = 4 nm and $D_{\max}$ = 12 nm, whereas the PX407-DMPC system exhibited larger dimensions (R_g = 13 nm, $D_{\max}$ = 38 nm) (Table 2). For the SMA system, the low-s region ($s < 0.2$ nm^{-1}) was excluded from the IFT analysis due to increased scattering intensity, likely caused by residual or aggregated liposomes. While both systems displayed characteristic bilayer peaks, their $p(r)$ functions differed significantly in shape and extent, indicating fundamental differences in their assembly structures.

SAXS Analysis of PX407/SMA-DMPC Systems: IFT Assuming Flat Structures. To elucidate the membrane structure, SAXS data were analyzed under the assumption of flat structures. Figure S3a−d show the scattering curves and the theoretical curves obtained from IFT analysis, assuming flat structures for the PX407-DMPC and SMA-DMPC systems. The agreement between the experimental data and the theoretical curves supported the validity of this analytical approach. Figure S3e−h present the thickness pair-distance distribution functions, $p_t(r)$, obtained through the IFT analysis. The membrane thickness values (T) determined from the IFT analysis were greater for the PX407-DMPC system (T = 5.5 nm) than for the SMA-DMPC system (T = 5.0 nm) (Table 2).

SAXS Analysis of PX407/SMA-DMPC Systems: Validation of Discoidal Structure Model. Based on the similarity of scattering profiles between the PX407-DMPC and SMA-DMPC systems, we hypothesized a discoidal structure for the PX407-DMPC assemblies and evaluated this assumption. Using the $D_{\max}$ and T parameters obtained from standard IFT analysis and IFT analysis assuming flat structures, respectively, the diameter (D) of a homogeneous discoidal structure was calculated using the Pythagorean theorem as $D = \sqrt{D_{\max}^2 - T^2}$. For particles with a homogeneous discoidal structure of diameter D and thickness T, the radius of gyration (R_g^{disc}) was calculated using eq 5 (Table 2). A comparison between theoretically calculated R_g^{disc} and R_g obtained from standard IFT analysis showed good agreement for all samples, supporting the hypothesis that the PX407-DMPC system exhibits a discoidal structure. For reference, assuming a hollow sphere structure with thickness T instead of a discoidal structure resulted in theoretically calculated R_g values that did not align with those obtained from standard IFT analysis (data not shown). Similarly, assuming a hollow cylinder structure required a membrane curvature too high for stable existence to achieve agreement between theoretical and IFT-derived R_g values (data not shown). It should be noted

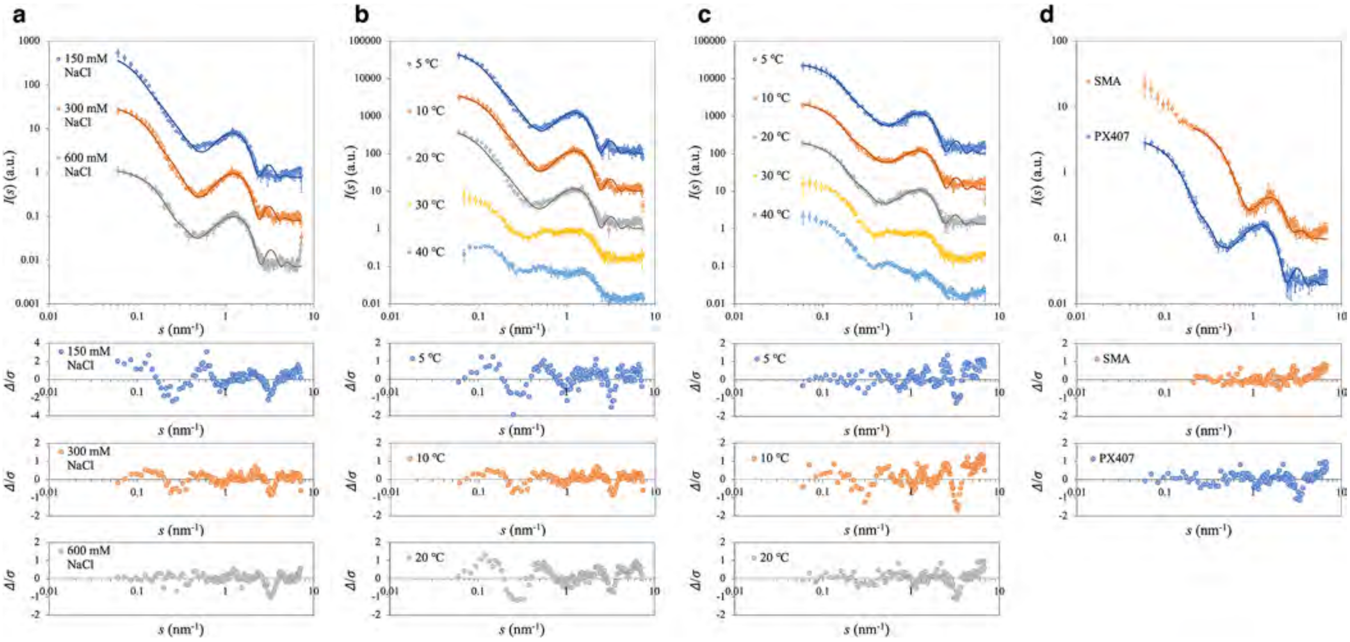

Figure 4. SAXS profiles and core–shell bicelle-belt (CSBB) model fitting results, along with residual plots, for PX407-DMPC and SMA-DMPC systems under various conditions. The upper panels present SAXS profiles (dots) overlaid with the theoretical scattering curves (solid lines) calculated from CSBB modeling, while the lower panels display the normalized residual plots (Δ/σ) for each condition. SAXS profiles are presented as mean ± standard deviation ($n = 3$). Normalized residuals (Δ/σ) were calculated using standard error propagation, accounting for both statistical and experimental uncertainties. (a) Effect of NaCl concentration (150, 300, and 600 mM) on PX407-DMPC systems (1:1 mass ratio) at 10 °C. (b) Effect of temperature (5–40 °C) on PX407-DMPC systems (PX407: DMPC = 1:1 mass ratio) in 300 mM NaCl. (c) Effect of temperature (5–40 °C) on PX407-DMPC systems (PX407: DMPC = 2:1 mass ratio) in 300 mM NaCl. (d) Effect of amphiphilic polymer type (SMA vs PX407) on polymer-DMPC systems (polymer: DMPC = 2:1 mass ratio) in 300 mM NaCl at 20 °C. The concentrations of DMPC were 7.4–9.6 mg/mL for PX407-DMPC systems and 3.65 mg/mL for SMA-DMPC system.

Table 3. Estimated Dimensions Obtained from Core–Shell Bicelle-Belt (CSBB) Modeling for SAXS Data

					SAXS data				
					core–shell bicelle-belt (CSBB) model[a]				
polymer	lipid	NaCl conc. (mM)	mass ratio (polymer: lipid)	temperature (°C)	R (nm) (polydispersity)	t_{rim} (nm)	t_{face} (nm)	L (nm)	volume ratio (rim: core + face)
PX407	DMPC	150	1:1	10	15.0 (0.12)	14.5	0.9	3.0	1.8:1
PX407	DMPC	300	1:1	10	13.1 (0.02)	10.1	0.9	3.0	1.3:1
PX407	DMPC	600	1:1	10	9.0 (0.18)	6.3	0.7	2.9	1.2:1
PX407	DMPC	300	1:1	5	14.4 (0.00)	11.8	0.9	3.0	1.4:1
PX407	DMPC	300	1:1	10	13.1 (0.02)	10.1	0.9	3.0	1.3:1
PX407	DMPC	300	1:1	20	15.9 (0.16)	10.8	0.8	3.0	1.2:1
PX407	DMPC	300	1:1	30	N.A.	N.A.	N.A.	N.A.	N.A.
PX407	DMPC	300	1:1	40	N.A.	N.A.	N.A.	N.A.	N.A.
PX407	DMPC	300	2:1	5	8.5 (0.25)	8.6	0.8	2.9	2.0:1
PX407	DMPC	300	2:1	10	9.3 (0.22)	8.5	0.7	3.0	1.8:1
PX407	DMPC	300	2:1	20	9.8 (0.07)	8.5	0.8	3.0	1.6:1
PX407	DMPC	300	2:1	30	N.A.	N.A.	N.A.	N.A.	N.A.
PX407	DMPC	300	2:1	40	N.A.	N.A.	N.A.	N.A.	N.A.
SMA	DMPC	300	2:1	20	2.7 (0.40)	1.2	0.9	2.5	0.6:1
PX407	DMPC	300	2:1	20	9.8 (0.07)	8.5	0.8	3.0	1.6:1

[a] Described in Figure 1b.

that distinguishing between circular and elliptical cross sections based solely on R_g value comparisons would be challenging.

SAXS Analysis of PX407/SMA-DMPC Systems: Discoidal Structure Modeling Analysis. To elucidate detailed structural features, we conducted fitting analyses using the CSBB model, which assumes PX407 binding to the disc edges. Figure 4a–d display the experimental scattering curves alongside the theoretical curves derived from the fitting analysis. The plots below each scattering profile illustrate the normalized residuals between the experimental data and theoretical predictions. The CSBB model produced good fits to the experimental data across all examined conditions: varying salt concentrations (Figure 4a), temperatures below the T_m at both 1:1 (Figure 4b) and 2:1 (Figure 4c) PX407: DMPC mass ratios, and comparisons with the SMA system (Figure 4d). However, some systematic deviations were observed under low salt concentration (150 mM) and PX407: DMPC = 1:1 conditions, indicating potential instability of the discoidal structures and system inhomogeneity under these conditions. As a reference, CSBB model analysis assuming elliptical geometry yielded nearly identical major and minor axis values, supporting our assumption of a circular cross-section (data not shown).

The CSBB model parameters provided quantitative insights into the structural features of the discoidal assemblies (Table 3). At a fixed PX407: DMPC mass ratio of 1:1 and a temperature of 10 °C, the core radius (R) and rim thickness (t_{rim}) strongly depended on salt concentration. At 300 mM NaCl, R and t_{rim} were determined to be 13.1 and 10.1 nm, respectively. The core thickness (L) and face layer thickness (t_{face}) remained relatively constant across all conditions examined (L = 2.9–3.0 nm, t_{face} = 0.7–0.9 nm), consistent with the typical dimensions of DMPC bilayers. As the NaCl concentration increased from 150 to 600 mM, both R and t_{rim} systematically decreased: R reduced from 15.0 to 9.0 nm, and t_{rim} decreased from 14.5 to 6.3 nm, indicating more compact structures at higher salt concentrations. This structural compression was reflected in the rim-to-(core+face) volume ratio (i.e., PX407-to-DMPC volume ratio), which decreased from 1.8:1 to 1.2:1 as NaCl concentration increased from 150 to 600 mM. The reduced ratio suggested a decrease in the amount of PX407 required to solubilize a given amount of DMPC. These findings indicated enhanced binding of PX407 to DMPC at higher salt concentrations. Additionally, the ratio of $L/2$ to t_{face}, corresponding to the DMPC tail and head regions, was determined to be 1.7–2.0, which closely matched the reported ratio for DMPC liposomes at 18 °C (1.8–2.3).[56]

The effect of polymer content became evident when comparing the 1:1 and 2:1 PX407: DMPC mass ratios at 300 mM NaCl. The 2:1 ratio produced smaller and more uniform structures, with R values ranging from 8.5 to 9.8 nm and a consistent t_{rim} of approximately 8.5 nm across 5–20 °C. In contrast, the 1:1 mass ratio exhibited greater variability, with R ranging from 13.1 to 15.9 nm and t_{rim} ranging from 10.1 to 11.8 nm over the same temperature range. Interestingly, the higher polymer content in the 2:1 mass ratio resulted in larger rim-to-(core + face) volume ratios (1.6–2.0:1) compared to the 1:1 mass ratio (1.2–1.4:1), indicating more extensive polymer coverage of the disc edges. This enhanced polymer coverage likely contributed to the improved stability observed in the 2:1 mass ratio systems.

Under identical conditions (2:1 mass ratio, 300 mM NaCl, 20 °C), the PX407-DMPC system exhibited significantly larger dimensions (R = 9.8 nm, t_{rim} = 8.5 nm) compared to the SMA-DMPC system (R = 2.7 nm, t_{rim} = 1.2 nm). While the face layer thickness (t_{face}) was similar between the two systems (t_{face} = 0.8–0.9 nm), the core thickness (L) was smaller for the SMA-DMPC system (L = 2.5 nm) than for the PX407-DMPC system (L = 3.0 nm), suggesting a more compact organization of the acyl chain region in the SMA-DMPC system. This observation aligned with the results of IFT analysis, which assumed flat structural arrangements. The total thickness ($2t_{\mathrm{face}} + L$) of the SMA-DMPC and PX407-DMPC systems was calculated to be 4.3 and 4.6 nm, respectively. The thickness values of the two systems were nearly identical and closely approximated that of conventional DMPC bilayers, making it challenging to determine which system more accurately replicated the bilayer structure. However, considering that the peak position in the SAXS profile of the PX407-DMPC system corresponded closely to that of DMPC liposomes, the PX407 system likely possessed a thickness more similar to conventional lipid bilayers. The rim-to-(core+face) volume ratio differed significantly between the two systems, with values of 1.6:1 for PX407-DMPC and 0.6:1 for SMA-DMPC, indicating distinct modes of interaction with DMPC. Additionally, the polydispersity of R was substantially higher for the SMA-DMPC system (0.40) compared to the PX407-DMPC system (0.07), suggesting less uniform particle formation in the SMA-DMPC system. This difference may also reflect SMA's reported ability to bind not only to the acyl chains but partially to the polar headgroups of DMPC, as previously described.[54] This binding characteristic likely complicated the strict application of the CSBB model to the SMA-DMPC system.

TEM Observation of PX407-DMPC Systems. To validate the CSBB model analysis of SAXS data, negative-stain TEM images were obtained at 23 °C for PX407: DMPC = 1:1 mass ratio in both 300 mM NaCl and 600 mM NaCl conditions (Figure 5a,b). Samples were observed after 5-fold dilution with the corresponding buffers. The TEM images revealed a mixture of circular particles along with elongated rod-like or elliptical particles. These varied morphologies can be attributed to different viewing orientations of the LNDs. Specifically, circular particles likely represent LNDs viewed from top or bottom faces, while rod-like or elliptical particles correspond to side or oblique views of the LNDs.

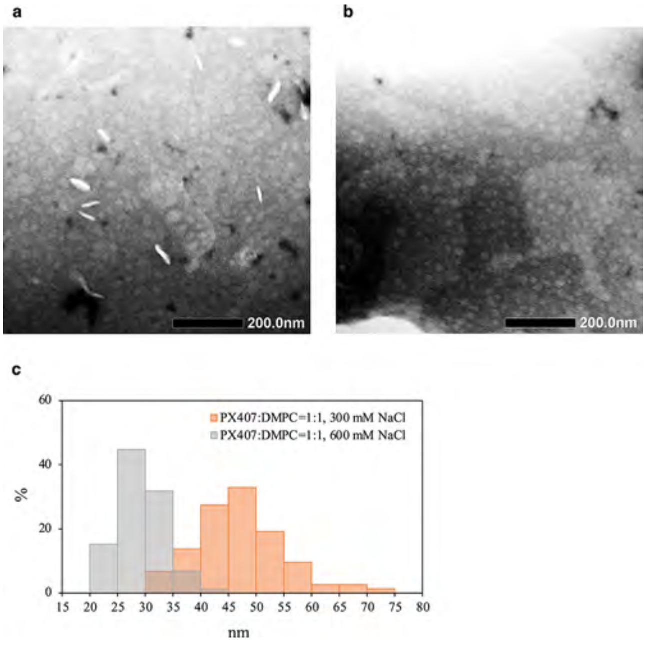

Figure 5. (a,b) Negative-stain TEM images and (c) particle size distributions. (a) PX407: DMPC = 1:1 mass ratio in 300 mM NaCl, (b) PX407: DMPC = 1:1 mass ratio in 600 mM NaCl. TEM observation was performed at 23 °C after 5-fold dilution of the samples with the corresponding buffers. Particle sizes were determined by circular approximation of the particles in TEM images, and the size distributions were obtained from 85 particles. The mean particle size ± standard deviation was 45.9 ± 8.3 nm for PX407: DMPC = 1:1 mass ratio in 300 mM NaCl, and 29.2 ± 4.0 nm for PX407: DMPC = 1:1 mass ratio in 600 mM NaCl. Scale bar: (a,b) 200.0 nm.

For quantitative particle size analysis, measurements were performed on 85 particles using circular approximation in the

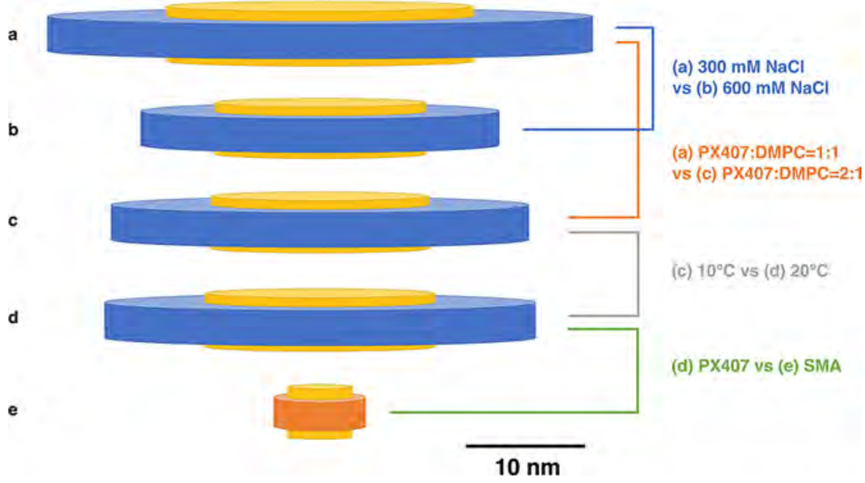

Figure 6. Size comparison of polymer-DMPC lipid nanodiscs (LNDs) with different compositions and conditions, based on structural parameters determined from core−shell bicelle-belt (CSBB) model analysis. (a) PX407: DMPC = 1:1 mass ratio in 300 mM NaCl at 10 °C, (b) PX407: DMPC = 1:1 mass ratio in 600 mM NaCl at 10 °C, (c) PX407: DMPC = 2:1 mass ratio in 300 mM NaCl at 10 °C, (d) PX407: DMPC = 2:1 mass ratio in 300 mM NaCl at 20 °C, and (e) SMA: DMPC = 2:1 mass ratio in 300 mM NaCl at 20 °C. Colored brackets indicate different effects: blue for NaCl concentration, orange for polymer-to-DMPC ratio, gray for temperature, and green for polymer type. Scale bar: 10 nm.

TEM images (Figure 5c). The mean particle diameter was determined to be 45.9 ± 8.3 nm for the 300 mM NaCl condition and 29.2 ± 4.0 nm for the 600 mM NaCl condition. These values show good agreement with the diameters derived from the CSBB model analysis of SAXS data (53.4 and 30.6 nm, respectively). This experimental concordance supports the validity of the CSBB model applied to the PX407-DMPC systems. Analysis of particle size distributions revealed a narrower distribution for the 600 mM NaCl condition compared to the 300 mM NaCl condition. This finding confirms the enhanced system homogeneity with increasing salt concentration, as predicted by the CSBB model analysis of SAXS data.

Compared to typical nanodisc TEM images,[57−59] the PX407-DMPC systems exhibited characteristically indistinct particle contours. While optimization of experimental conditions might offer some improvement, this feature may be attributed to the inherent properties of PX407. One possible explanation is that the staining agent penetrates into the hydrophilic block regions of PX407 that constitute the disc belt, resulting in blurred contours. Additionally, the intrinsic heterogeneity of PX407 itself, including molecular weight distribution, may also contribute to this observation.

Structural Characteristics of PX407-DMPC LNDs. In summary, the CSBB model analysis revealed distinct structural characteristics of LNDs for both PX407 (blue) and SMA (orange) systems, as illustrated in Figure 6. The dimensions of PX407-DMPC LNDs were found to be modulated by salt concentration and polymer-to-lipid ratio: increasing NaCl concentration reduced the core radius and rim thickness [(a) vs (b)], while a higher PX407: DMPC mass ratio (2:1) resulted in more compact structures compared to the 1:1 mass ratio [(a) vs (c)]. Below the T_m of DMPC (approximately 24 °C), the structural parameters remained largely unchanged as the temperature increased from 10 to 20 °C at PX407: DMPC = 2:1 [(c) vs (d)]. Notably, under identical conditions (polymer: DMPC = 2:1, 300 mM NaCl, 20 °C), PX407-DMPC LNDs [(d)] exhibited significantly larger dimensions than SMA-DMPC LNDs [(e)], with approximately 3.6-fold larger core radius and a 7.1-fold thicker rim region. These systematic investigations provided detailed insights into the structure and characteristics of PX407-DMPC LNDs, highlighting their tunable dimensions and structural stability under controlled conditions.

It should be noted that the structural information obtained through the CSBB model analysis represents the average characteristics of the particles. While the PX407-DMPC systems show relatively narrow size distributions, they still exhibits some degree of polydispersity. This variability is supported by the particle size distributions from DLS measurements (PDI: 0.20−0.30) and the diameter distributions obtained from TEM images. Additionally, residual analysis of the CSBB model fitting revealed larger deviations for the PX407: DMPC = 1:1 condition compared to the 2:1 condition, with this trend becoming more pronounced at lower salt concentrations (i.e., 150 mM NaCl). These results suggest that the particle size distribution is broader, particularly under the PX407: DMPC = 1:1 and low salt concentration conditions. Furthermore, these conditions may contain small amounts of DMPC vesicles that were not completely transformed into LNDs by PX407. These factors likely contribute to the reduced accuracy of the CSBB model analysis under these specific conditions.

This study did not elucidate the exact orientation of PX407 binding to the DMPC bilayer. However, it can be hypothesized that the hydrophobic PPO segment binds to the acyl chains, while the hydrophilic PEO segments resides within the rim volume. Assuming average degrees of polymerization (i.e., a(PEO) = 101, b(PPO) = 56), the maximum lengths of the PEO and PPO segments (in a fully extended linear conformation) were estimated to be approximately 36 and 20 nm, respectively. These values were calculated using the C−C bond length (1.54 Å), C−O bond length (1.43 Å), and bond angle (109.5°). Given that the rim thickness (t_{rim}) ranges from 6.3 to 14.5 nm—less than the maximum length of the PEO segment (∼36 nm)—it can be postulated that the PEO segment adopts a folded conformation within the rim volume. In contrast, the core thickness (L) ranges from 2.9 to 3.0 nm, which is much smaller than the maximum length of the PPO segment (∼20 nm). Therefore, it can be hypothesized that if the PPO segment binds parallel to the acyl chains (i.e., perpendicular to the bilayer), it likely adopts a "picket fence" conformation. Alternatively, if the PPO segment binds perpendicular to the acyl chains (i.e., parallel to the bilayer), it could adopt a belt-like conformation. Given that the circumference of the DMPC bilayer edge (i.e., the perimeter) was calculated to be 53.4−94.2 nm from the core radius (R = 8.5−15.0 nm)—which exceeds the maximum length of the PPO segment (~20 nm)—multiple PX407 molecules would need to cooperatively wrap around the DMPC bilayer if PX407 adopts a belt-like conformation. Further investigations are required to elucidate the detailed binding mode of PX407.

Potential Applications and Limitations of PX407-DMPC LNDs. Structural characterization revealed both advantages and limitations of PX407-DMPC LNDs for potential applications. Notably, these LNDs exhibited larger dimensions compared to conventional SMA-DMPC LNDs, with core diameters reaching approximately 20 nm under optimal conditions (300 mM NaCl, PX407: DMPC ≥ 1:1 mass ratio). These larger dimensions could be advantageous for reconstituting membrane proteins with large extramembrane domains or oligomeric complexes that require extensive lipid platforms. Moreover, the ability to control LND size by adjusting salt concentration and the polymer-to-lipid ratio provides flexibility in tailoring the system for specific applications.

However, the temperature-dependent stability of these LNDs, particularly their destabilization above the T_m of DMPC (approximately 24 °C), presents both limitations and opportunities. While this thermal sensitivity may restrict their use in applications requiring elevated temperatures, it could be exploited for temperature-triggered release in drug delivery systems. For example, local heating could enable controlled disassembly of the LNDs, potentially allowing site-specific release of encapsulated therapeutic agents. The formation of uniform and stable LNDs at temperatures below 20 °C, especially at higher PX407: DMPC ratios, suggests potential applications as drug delivery systems for temperature-sensitive therapeutic agents. Additionally, FDA guide has presented PX as an "inactive" ingredient for different types of preparations (e.g., intravenous, inhalation, oral solutions, suspensions, ophthalmic, and topical formulations).[60,61] These characteristics could facilitate the practical implementation of these systems.

Future studies could optimize the system through several strategies, including: incorporation of PLs with higher T_m (e.g., DPPC); introduction of charged PLs to improve particle dispersibility; use of PXs with a higher PPO content (e.g., PX237) to enhance solubilization capability; and development of modified PX derivatives to improve thermal stability. Additionally, investigating the compatibility of these LNDs with various membrane proteins and their potential for targeted drug delivery would be valuable for expanding their practical applications.

CONCLUSIONS

In this study, we performed comprehensive structural characterization of PX407-DMPC LNDs using SAXS analysis combined with turbidity assessment and TEM observation. The results demonstrated that PX407, with the highest proportion of hydrophobic PPO segment among the tested PXs, effectively solubilized DMPC to form discoidal nanostructures. The size of these LNDs could be systematically controlled by adjusting the salt concentration and polymer-to-lipid ratio, with core diameters ranging from approximately 17−30 nm. The structural stability was notably enhanced at higher polymer content (PX407: DMPC = 2:1 mass ratio) and salt concentrations (≥300 mM NaCl), although they appeared to be unstable above the T_m of DMPC (approximately 24 °C).

Comparative analysis with SMA-DMPC LNDs revealed that PX407-DMPC LNDs exhibited distinct structural features, maintaining a membrane thickness closer to that of conventional DMPC bilayers while having larger dimensions than typical LNDs. The detailed structural information obtained through CSBB model analysis provides fundamental insights into the polymer−lipid organization within these systems. However, the binding mode of PX407 to the DMPC bilayer—whether in a picket fence conformation perpendicular to the bilayer or in a belt-like conformation parallel to it—remains to be clarified in future studies. The findings of this study not only enhance our understanding of PX−PL interactions but also suggest potential applications of PX407-DMPC LNDs in various fields, particularly in systems requiring larger membrane protein platforms or temperature-responsive behavior.

ASSOCIATED CONTENT

Supporting Information

The Supporting Information is available free of charge at https://pubs.acs.org/doi/10.1021/acs.langmuir.5c01675.

> Particle size number distribution of poloxamer-phosphatidylcholine mixtures analyzed by DLS (Figure S1), DLS autocorrelation functions and cumulant fitting results for poloxamer-phospholipid mixtures (Figure S2), and SAXS profiles and thickness pair-distance distribution functions $p_t(r)$ of PX407-DMPC systems (Figure S3) (PDF)

AUTHOR INFORMATION

Corresponding Authors

Masakazu Fukuda − *Laboratory of Functional Molecular Chemistry, Kobe Pharmaceutical University, Kobe 658-8558, Japan;* Present Address: : Formulation Development Department, Chugai Pharmaceutical Co., Ltd., 5-5-1 Ukima, Kita-ku, Tokyo 115-8543, Japan; orcid.org/0000-0003-1979-9265; Email: fukuda.masakazu43@chugai-pharm.co.jp, mnkt1981@gmail.com

Masafumi Tanaka − *Laboratory of Functional Molecular Chemistry, Kobe Pharmaceutical University, Kobe 658-8558, Japan;* orcid.org/0000-0001-6917-7822; Email: masatnk@kobepharma-u.ac.jp

Authors

Yuichi Takasaki − *Business Unit Characterization, Anton Paar Japan K.K., Tokyo 131-0034, Japan*

Mizuho Ichihara − *Laboratory of Functional Molecular Chemistry, Kobe Pharmaceutical University, Kobe 658-8558, Japan*

Toru Takarada − *Laboratory of Functional Molecular Chemistry, Kobe Pharmaceutical University, Kobe 658-8558, Japan;* orcid.org/0000-0001-9993-4433

Keisuke Ikeda − *Department of Biointerface Chemistry, Faculty of Pharmaceutical Sciences, University of Toyama, Toyama 930-0194, Japan;* orcid.org/0000-0003-3217-5713

Minoru Nakano − *Department of Biointerface Chemistry, Faculty of Pharmaceutical Sciences, University of Toyama, Toyama 930-0194, Japan;* orcid.org/0000-0003-2688-1347

Complete contact information is available at:
https://pubs.acs.org/10.1021/acs.langmuir.5c01675

Author Contributions

M.F.: conceptualization, methodology, investigation, writing—original draft, supervision. Y.T.: methodology, investigation, writing—review and editing. M.I.: investigation, writing—review and editing. T.T.: writing—review and editing. K.I.: methodology, investigation, writing—review and editing. M.N.: methodology, writing—review and editing. M.T.: resources, writing—review and editing, project administration.

Notes

The authors declare no competing financial interest.

■ ACKNOWLEDGMENTS

The authors acknowledge Shinichi Nabekura (Reifycs Analytical Inc.) for facilitating access to the dynamic light scattering equipment.

■ ABBREVIATIONS

CSBB, core−shell bicelle-belt; DMPC, 1,2-dimyristoyl-*sn*-glycero-3-phosphocholine; T_m, gel-to-liquid crystalline phase transition temperature; HDL, high-density lipoprotein; IFT, indirect Fourier transformation; LND, lipid nanodisc; MSP, membrane scaffold protein; POPC, 1-palmitoyl-2-oleoyl-*sn*-glycero-3-phosphocholine; PL, phospholipid; PX, poloxamer; PDI, polydispersity index; PEO, poly(ethylene oxide); PPO, poly(propylene oxide); SLD, scattering length density; $p(r)$, pair-distance distribution function; $p_t(r)$, thickness pair-distance distribution function; SMA, styrene-maleic acid; TEM, transmission electron microscopy

■ REFERENCES

(1) Tanaka, M. Applications of Synthetic Polymer Discoidal Lipid Nanoparticles to Biomedical Research. *Chem. Pharm. Bull. (Tokyo)* **2022**, *70* (8), 507−513.

(2) Elzoghby, A. O.; Samir, O.; Soliman, A.; Solomevich, S.; Yu, M.; Schwendeman, A.; Nasr, M. L. Nanodiscs: Game Changer Nano-Therapeutics and Structural Biology Tools. *Nano Today* **2023**, *53*, No. 102026.

(3) Dong, Y.; Tang, H.; Dai, H.; Zhao, H.; Wang, J. The Application of Nanodiscs in Membrane Protein Drug Discovery & Development and Drug Delivery. *Front. Chem.* **2024**, *12*, No. 1444801.

(4) Jonas, A.; Kézdy, K. E.; Wald, J. H. Defined Apolipoprotein A-I Conformations in Reconstituted High Density Lipoprotein Discs. *J. Biol. Chem.* **1989**, *264* (9), 4818−4824.

(5) Segrest, J. P.; Jones, M. K.; Klon, A. E.; Sheldahl, C. J.; Hellinger, M.; De Loof, H.; Harvey, S. C. A Detailed Molecular Belt Model for Apolipoprotein A-I in Discoidal High Density Lipoprotein. *J. Biol. Chem.* **1999**, *274* (45), 31755−31758.

(6) Tanaka, M.; Dhanasekaran, P.; Nguyen, D.; Ohta, S.; Lund-Katz, S.; Phillips, M. C.; Saito, H. Contributions of the N- and C-Terminal Helical Segments to the Lipid-Free Structure and Lipid Interaction of Apolipoprotein A-I. *Biochemistry* **2006**, *45* (34), 10351−10358.

(7) Nakano, M.; Fukuda, M.; Kudo, T.; Miyazaki, M.; Wada, Y.; Matsuzaki, N.; Endo, H.; Handa, T. Static and Dynamic Properties of Phospholipid Bilayer Nanodiscs. *J. Am. Chem. Soc.* **2009**, *131* (23), 8308−8312.

(8) Fukuda, M.; Nakano, M.; Miyazaki, M.; Handa, T. Thermodynamic and Kinetic Stability of Discoidal High-Density Lipoprotein Formation from Phosphatidylcholine/Apolipoprotein A-I Mixture. *J. Phys. Chem. B* **2010**, *114* (24), 8228−8234.

(9) Phillips, M. C. New Insights into the Determination of HDL Structure by Apolipoproteins: Thematic Review Series: High Density Lipoprotein Structure, Function, and Metabolism. *J. Lipid Res.* **2013**, *54* (8), 2034−2048.

(10) Melchior, J. T.; Walker, R. G.; Cooke, A. L.; Morris, J.; Castleberry, M.; Thompson, T. B.; Jones, M. K.; Song, H. D.; Rye, K.-A.; Oda, M. N.; Sorci-Thomas, M. G.; Thomas, M. J.; Heinecke, J. W.; Mei, X.; Atkinson, D.; Segrest, J. P.; Lund-Katz, S.; Phillips, M. C.; Davidson, W. S. A Consensus Model of Human Apolipoprotein A-I in Its Monomeric and Lipid-Free State. *Nat. Struct. Mol. Biol.* **2017**, *24* (12), 1093−1099.

(11) Denisov, I. G.; Grinkova, Y. V.; Lazarides, A. A.; Sligar, S. G. Directed Self-Assembly of Monodisperse Phospholipid Bilayer Nanodiscs with Controlled Size. *J. Am. Chem. Soc.* **2004**, *126* (11), 3477−3487.

(12) Whorton, M. R.; Bokoch, M. P.; Rasmussen, S. G. F.; Huang, B.; Zare, R. N.; Kobilka, B.; Sunahara, R. K. A Monomeric G Protein-Coupled Receptor Isolated in a High-Density Lipoprotein Particle Efficiently Activates Its G Protein. *Proc. Natl. Acad. Sci. U.S.A.* **2007**, *104* (18), 7682−7687.

(13) Denisov, I. G.; Sligar, S. G. Nanodiscs in Membrane Biochemistry and Biophysics. *Chem. Rev.* **2017**, *117* (6), 4669−4713.

(14) Dörr, J. M.; Koorengevel, M. C.; Schäfer, M.; Prokofyev, A. V.; Scheidelaar, S.; van der Cruijsen, E. A. W.; Dafforn, T. R.; Baldus, M.; Killian, J. A. Detergent-Free Isolation, Characterization, and Functional Reconstitution of a Tetrameric K^+ Channel: The Power of Native Nanodiscs. *Proc. Natl. Acad. Sci. U.S.A.* **2014**, *111* (52), 18607−18612.

(15) Sligar, S. G.; Denisov, I. G. Nanodiscs: A Toolkit for Membrane Protein Science. *Protein Sci.* **2021**, *30* (2), 297−315.

(16) Padmanabha Das, K. M.; Shih, W. M.; Wagner, G.; Nasr, M. L. Large Nanodiscs: A Potential Game Changer in Structural Biology of Membrane Protein Complexes and Virus Entry. *Front. Bioeng. Biotechnol* **2020**, *8*, 539.

(17) Grinkova, Y. V.; Denisov, I. G.; Sligar, S. G. Engineering Extended Membrane Scaffold Proteins for Self-Assembly of Soluble Nanoscale Lipid Bilayers. *Protein Eng. Des. Sel.* **2010**, *23* (11), 843−848.

(18) Knowles, T. J.; Finka, R.; Smith, C.; Lin, Y.-P.; Dafforn, T.; Overduin, M. Membrane Proteins Solubilized Intact in Lipid Containing Nanoparticles Bounded by Styrene Maleic Acid Copolymer. *J. Am. Chem. Soc.* **2009**, *131* (22), 7484−7485.

(19) Orwick, M. C.; Judge, P. J.; Procek, J.; Lindholm, L.; Graziadei, A.; Engel, A.; Gröbner, G.; Watts, A. Detergent-Free Formation and Physicochemical Characterization of Nanosized Lipid-Polymer Complexes: Lipodisq. *Angew. Chem., Int. Ed. Engl.* **2012**, *51* (19), 4653−4657.

(20) Dörr, J. M.; Scheidelaar, S.; Koorengevel, M. C.; Dominguez, J. J.; Schäfer, M.; van Walree, C. A.; Killian, J. A. The Styrene−Maleic Acid Copolymer: A Versatile Tool in Membrane Research. *Eur. Biophys. J.* **2016**, *45* (1), 3−21.

(21) Oluwole, A. O.; Danielczak, B.; Meister, A.; Babalola, J. O.; Vargas, C.; Keller, S. Solubilization of Membrane Proteins into Functional Lipid-Bilayer Nanodiscs Using a Diisobutylene/Maleic Acid Copolymer. *Angew. Chem., Int. Ed. Engl.* **2017**, *56* (7), 1919−1924.

(22) Yasuhara, K.; Arakida, J.; Ravula, T.; Ramadugu, S. K.; Sahoo, B.; Kikuchi, J.-I.; Ramamoorthy, A. Spontaneous Lipid Nanodisc Fomation by Amphiphilic Polymethacrylate Copolymers. *J. Am. Chem. Soc* **2017**, *139* (51), 18657−18663.

(23) Hardin, N. Z.; Ravula, T.; Mauro, G. D.; Ramamoorthy, A. Hydrophobic Functionalization of Polyacrylic Acid as a Versatile Platform for the Development of Polymer Lipid Nanodisks. *Small* **2019**, *15* (9), No. e1804813.

(24) Ravula, T.; Ramadugu, S. K.; Di Mauro, G.; Ramamoorthy, A. Bioinspired, Size-tunable Self-assembly of Polymer−Lipid Bilayer

Nanodiscs. *Angew. Chem. Weinheim Bergstr. Ger.* **2017**, *129* (38), 11624−11628.

(25) Nasr, M. L.; Baptista, D.; Strauss, M.; Sun, Z.-Y. J.; Grigoriu, S.; Huser, S.; Plückthun, A.; Hagn, F.; Walz, T.; Hogle, J. M.; Wagner, G. Covalently Circularized Nanodiscs for Studying Membrane Proteins and Viral Entry. *Nat. Methods* **2017**, *14* (1), 49−52.

(26) Zhao, Z.; Zhang, M.; Hogle, J. M.; Shih, W. M.; Wagner, G.; Nasr, M. L. DNA-Corralled Nanodiscs for the Structural and Functional Characterization of Membrane Proteins and Viral Entry. *J. Am. Chem. Soc.* **2018**, *140* (34), 10639−10643.

(27) Perrault, S. D.; Walkey, C.; Jennings, T.; Fischer, H. C.; Chan, W. C. W. Mediating Tumor Targeting Efficiency of Nanoparticles Through Design. *Nano Lett.* **2009**, *9* (5), 1909−1915.

(28) Cabral, H.; Matsumoto, Y.; Mizuno, K.; Chen, Q.; Murakami, M.; Kimura, M.; Terada, Y.; Kano, M. R.; Miyazono, K.; Uesaka, M.; Nishiyama, N.; Kataoka, K. Accumulation of Sub-100 Nm Polymeric Micelles in Poorly Permeable Tumours Depends on Size. *Nat. Nanotechnol.* **2011**, *6* (12), 815−823.

(29) Champion, J. A.; Katare, Y. K.; Mitragotri, S. Particle Shape: A New Design Parameter for Micro- and Nanoscale Drug Delivery Carriers. *J. Controlled Release* **2007**, *121* (1−2), 3−9.

(30) Decuzzi, P.; Godin, B.; Tanaka, T.; Lee, S.-Y.; Chiappini, C.; Liu, X.; Ferrari, M. Size and Shape Effects in the Biodistribution of Intravascularly Injected Particles. *J. Controlled Release* **2010**, *141* (3), 320−327.

(31) Oda, M. N.; Hargreaves, P. L.; Beckstead, J. A.; Redmond, K. A.; van Antwerpen, R.; Ryan, R. O. Reconstituted High Density Lipoprotein Enriched with the Polyene Antibiotic Amphotericin B. *J. Lipid Res.* **2006**, *47* (2), 260−267.

(32) Ghosh, M.; Singh, A. T. K.; Xu, W.; Sulchek, T.; Gordon, L. I.; Ryan, R. O. Curcumin Nanodisks: Formulation and Characterization. *Nanomedicine* **2011**, *7* (2), 162−167.

(33) Yuan, Y.; Wen, J.; Tang, J.; Kan, Q.; Ackermann, R.; Olsen, K.; Schwendeman, A. Synthetic High-Density Lipoproteins for Delivery of 10-Hydroxycamptothecin. *Int. J. Nanomed.* **2016**, *11*, 6229−6238.

(34) Torgersen, M. L.; Judge, P. J.; Bada Juarez, J. F.; Pandya, A. D.; Fusser, M.; Davies, C. W.; Maciejewska, M. K.; Yin, D. J.; Maelandsmo, G. M.; Skotland, T.; Watts, A.; Sandvig, K. Physicochemical Characterization, Toxicity and in Vivo Biodistribution Studies of a Discoidal, Lipid-Based Drug Delivery Vehicle: Lipodisq Nanoparticles Containing Doxorubicin. *J. Biomed. Nanotechnol.* **2020**, *16* (4), 419−431.

(35) Ghosh, M.; Ren, G.; Simonsen, J. B.; Ryan, R. O. Cationic Lipid Nanodisks as an siRNA Delivery Vehicle. *Biochem. Cell Biol.* **2014**, *92* (3), 200−205.

(36) He, W.; Evans, A. C.; Rasley, A.; Bourguet, F.; Peters, S.; Kamrud, K. I.; Wang, N.; Hubby, B.; Felderman, M.; Gouvis, H.; Coleman, M. A.; Fischer, N. O. Cationic HDL Mimetics Enhance in Vivo Delivery of Self-Replicating mRNA. *Nanomedicine* **2020**, *24*, No. 102154.

(37) Sharma, R.; Narum, S.; Liu, S.; Dong, Y.; Baek, K. I.; Jo, H.; Salaita, K. Nanodiscoidal Nucleic Acids for Gene Regulation. *ACS Chem. Biol.* **2023**, *18* (11), 2349−2367.

(38) Frias, J. C.; Ma, Y.; Williams, K. J.; Fayad, Z. A.; Fisher, E. A. Properties of a Versatile Nanoparticle Platform Contrast Agent to Image and Characterize Atherosclerotic Plaques by Magnetic Resonance Imaging. *Nano Lett.* **2006**, *6* (10), 2220−2224.

(39) Huda, P.; Binderup, T.; Pedersen, M. C.; Midtgaard, S. R.; Elema, D. R.; Kjær, A.; Jensen, M.; Arleth, L. PET/CT Based in Vivo Evaluation of 64Cu Labelled Nanodiscs in Tumor Bearing Mice. *PLoS One* **2015**, *10* (7), No. e0129310.

(40) Pérez-Medina, C.; Tang, J.; Abdel-Atti, D.; Hogstad, B.; Merad, M.; Fisher, E. A.; Fayad, Z. A.; Lewis, J. S.; Mulder, W. J. M.; Reiner, T. PET Imaging of Tumor-Associated Macrophages with 89Zr-Labeled High-Density Lipoprotein Nanoparticles. *J. Nucl. Med.* **2015**, *56* (8), 1272−1277.

(41) Chen, W.; Jarzyna, P. A.; van Tilborg, G. A. F.; Nguyen, V. A.; Cormode, D. P.; Klink, A.; Griffioen, A. W.; Randolph, G. J.; Fisher, E. A.; Mulder, W. J. M.; Fayad, Z. A. RGD Peptide Functionalized and Reconstituted High-Density Lipoprotein Nanoparticles as a Versatile and Multimodal Tumor Targeting Molecular Imaging Probe. *FASEB J.* **2010**, *24* (6), 1689−1699.

(42) Wu, G.; Khant, H. A.; Chiu, W.; Lee, K. Y. C. Effects of Bilayer Phases on Phospholipid-Poloxamer Interactions. *Soft Matter* **2009**, *5* (7), 1496.

(43) Wu, G.; Lee, K. Y. C. Interaction of Poloxamers with Liposomes: An Isothermal Titration Calorimetry Study. *J. Phys. Chem. B* **2009**, *113* (47), 15522−15531.

(44) Bartlett, G. R. Phosphorus Assay in Column Chromatography. *J. Biol. Chem.* **1959**, *234* (3), 466−468.

(45) Mayer, L. D.; Hope, M. J.; Cullis, P. R. Vesicles of Variable Sizes Produced by a Rapid Extrusion Procedure. *Biochim. Biophys. Acta* **1986**, *858* (1), 161−168.

(46) Mui, B.; Chow, L.; Hope, M. Extrusion Technique to Generate Liposomes of Defined Size. *Methods Enzymol.* **2003**, *367*, 3−14.

(47) Glatter, O. A New Method for the Evaluation of Small-Angle Scattering Data. *J. Appl. Crystallogr.* **1977**, *10* (5), 415−421.

(48) Glatter, O. Evaluation of Small-Angle Scattering Data from Lamellar and Cylindrical Particles by the Indirect Transformation Method. *J. Appl. Crystallogr.* **1980**, *13* (6), 577−584.

(49) Svergun, D. I.; Koch, M. H. J.; Timmins, P. A.; May, R. P. *Small Angle X-Ray and Neutron Scattering from Solutions of Biological Macromolecules*; Oxford University Press, International Union of Crystallography Texts on Crystallography, 2013.

(50) Jamshad, M.; Grimard, V.; Idini, I.; Knowles, T. J.; Dowle, M. R.; Schofield, N.; Sridhar, P.; Lin, Y.; Finka, R.; Wheatley, M.; Thomas, O. R. T.; Palmer, R. E.; Overduin, M.; Govaerts, C.; Ruysschaert, J.-M.; Edler, K. J.; Dafforn, T. R. Structural Analysis of a Nanoparticle Containing a Lipid Bilayer Used for Detergent-Free Extraction of Membrane Proteins. *Nano Res.* **2015**, *8* (3), 774−789.

(51) Maier, R.; Cuevas Arenas, R.; Zhang, F.; García-Sáez, A.; Schreiber, F. Structural Insights into Polymer-Bounded Lipid Nanodiscs. *Langmuir* **2023**, *39* (6), 2450−2459.

(52) Core_Shell_Bicelle_Elliptical_Belt_Rough—SasView 6.0.0 Documentation. https://www.sasview.org/docs/user/models/core_shell_bicelle_elliptical_belt_rough.html (accessed 2024-12-18).

(53) Kučerka, N.; Liu, Y.; Chu, N.; Petrache, H. I.; Tristram-Nagle, S.; Nagle, J. F. Structure of Fully Hydrated Fluid Phase DMPC and DLPC Lipid Bilayers Using X-Ray Scattering from Oriented Multilamellar Arrays and from Unilamellar Vesicles. *Biophys. J.* **2005**, *88* (4), 2626−2637.

(54) Tanaka, M.; Hosotani, A.; Tachibana, Y.; Nakano, M.; Iwasaki, K.; Kawakami, T.; Mukai, T. Preparation and Characterization of Reconstituted Lipid−Synthetic Polymer Discoidal Particles. *Langmuir* **2015**, *31* (46), 12719−12726.

(55) Feigin, L. A.; Svergun, D. I. Structure Analysis by Small-Angle X-Ray and Neutron Scattering; Taylor, G. W., Ed.; Springer: New York, NY, 2013 .

(56) Bjørnestad, V. A.; Orwick-Rydmark, M.; Lund, R. Understanding the Structural Pathways for Lipid Nanodisc Formation: How Styrene Maleic Acid Copolymers Induce Membrane Fracture and Disc Formation. *Langmuir* **2021**, *37* (20), 6178−6188.

(57) Grushin, K.; White, M. A.; Stoilova-McPhie, S. Reversible Stacking of Lipid Nanodiscs for Structural Studies of Clotting Factors. *Nanotechnol. Rev.* **2017**, *6* (1), 139−148.

(58) Larsen, A. H.; Johansen, N. T.; Gajhede, M.; Arleth, L.; Midtgaard, S. R. Lipid-Bound ApoE3 Self-Assemble into Elliptical Disc-Shaped Particles. *Biochim. Biophys. Acta Biomembr.* **2021**, *1863* (1), No. 183495.

(59) Mahler, F.; Meister, A.; Vargas, C.; Durand, G.; Keller, S. Self-Assembly of Protein-Containing Lipid-Bilayer Nanodiscs from Small-Molecule Amphiphiles. *Small* **2021**, *17* (49), No. e2103603.

(60) Rowe, R. C.; Sheskey, P.; Quinn, M. *Handbook of Pharmaceutical Excipients*; Libros Digitales-Pharmaceutical Press, 2009.

(61) Dumortier, G.; Grossiord, J. L.; Agnely, F.; Chaumeil, J. C. A Review of Poloxamer 407 Pharmaceutical and Pharmacological Characteristics. *Pharm. Res.* **2006**, *23* (12), 2709−2728.